Planetary and Space Science 224 (2022) 105593

Contents lists available at ScienceDirect

Planetary and Space Science

journal homepage: www.elsevier.com/locate/pss

Seasonal southern circum-polar spots and araneiforms observed with the colour and stereo surface imaging system (CaSSIS)

Camila Cesar [a,*], Antoine Pommerol [a], Nicolas Thomas [a], Ganna Portyankina [b], Candice J. Hansen [c], Livio L. Tornabene [d], Giovanni Munaretto [e], Gabriele Cremonese [e]

[a] Space Research and Planetology Division, Physikalisches Inst., Universität Bern, Switzerland
[b] University of Colorado, Boulder, USA
[c] Planetary Science Institute, St. George, USA
[d] Dept. of Earth Sciences, Western University, Inst. for Earth & Space Exploration, London, Canada
[e] INAF-Astronomical Observatory Padova, Padova, Italy

ARTICLE INFO

Keywords:
Mars
CaSSIS
Circum-polar
Seasonal
CO_2 ice

ABSTRACT

The southern polar area of Mars is home to various seasonal activity commonly explained by the Kieffer model. During southern spring, the ice covering the polar area sublimates and leaves distinct features (spiders, spots, fans) observable from orbit. The Colour and Stereo Surface Imaging System (CaSSIS) onboard the ExoMars Trace Gas Orbiter (TGO), provides high-resolution multi-filter images of the Martian surface offering high sensitivity to colour contrasts. Its stereo capability is pivotal for momentary processes and offers a unique perspective for studying surface sublimation processes and their relation to atmospheric features. For the first time, we identify clouds well correlated with surface features (araneiforms and spots at southern circum-polar latitudes) hence motivating a new campaign to refine these observations over time periods where CO_2 sublimation processes occur. We focus here on the structure of spot deposits and their evolution through time. We identify and describe seven structures: dark spot, bright-haloed spot, ringed spot, inverted spot, dark-haloed spot, banded spot, and bright spot. By morphological and spectral analyses, we hypothesize a new chronology of events that characterise the origin, formation and evolution of these features.

1. Introduction

1.1. Context

The aim of this study is to test the Kieffer hypothesis and provide an extended model of the formation and evolution of dune spots. We do this by using data from the Colour and Stereo Surface Imaging System (CaSSIS) acquired during winter, spring and summer, with regular repeated observation, consistent colours and variety of local solar time (LST). The dynamic processes, occurring during those times in the poles, can be observed. The cryptic region, defined as the low temperature (~150 K) and low albedo area in polar regions during springtime, has been mapped by MOC, TES and MOLA onboard the Mars Global Surveyor (MGS), suggesting the presence of a slab of translucent CO_2 ice (Kieffer et al., 2000; Kieffer, 2007). Inside this region, dark fans were observed together with fields of spots with haloes ("fried eggs"), and fields of radial erosion features ("spiders") centered near the core of fans (Kieffer, 2000; Kieffer et al., 2000, 2006; Piqueux et al., 2003; Titus et al., 1998, 2007). It was subsequently noticed that spiders show diverse morphologies (Hansen et al., 2010; Hao et al., 2019) and are not limited to this specific cryptic region (Schwamb et al., 2018).

The Kieffer model of CO_2 ice basal sublimation is commonly accepted as the explanation to the formation of dark spots and fans associated with araneiforms (Kieffer, 2000, 2007; Piqueux et al., 2003; Kieffer et al., 2006; Piqueux and Christensen, 2008; Hansen et al., 2010, 2017; Thomas et al., 2010, 2011b; Portyankina et al., 2010; Pilorget et al., 2011; Pommerol et al., 2011). During the cold winter nights, atmospheric CO_2 condensates at the surface in regions from the poles to latitudes ~50°. This dusty CO_2 frost undergoes a self-cleaning to form a translucent slab with dusty particles at its base. When the first light of spring arrives, the early low-grazing sunlight goes through the slab and heats up the dark dust particles. The thermal radiation, unable to escape because of the opaque characteristics of CO_2 ice at infrared wavelengths, builds-up heat leading to basal sublimation of the slab. This creates a pressure at the

* Corresponding author.
E-mail address: camila.cesar@unibe.ch (C. Cesar).

https://doi.org/10.1016/j.pss.2022.105593
Received 14 June 2021; Received in revised form 28 June 2022; Accepted 20 October 2022
Available online 1 November 2022

basal interface and, through weaknesses in the ice, CO_2 gas jets form carrying sand and dust.

The particles carried by the gas flow are deposited onto the surface forming spots or fans, that appear dark compared to the icy surroundings. Their shapes seem to be determined by the local topography and wind patterns as models suggest (Piqueux et al., 2003; Kieffer et al., 2006; Thomas et al., 2011a). The entire upper surface of the ice slab retreats because of constant sublimation and when the surface becomes ice-free, the centers of the araneiforms become more visible with the dark material previously on the ice blending in with the substrate (Piqueux et al., 2003; Aharonson et al., 2004; Kieffer et al., 2006; Kieffer, 2007).

The initial dark deposits on the ice have often been seen paired with brighter deposits, as seen on Fig. 3B. These bright deposits have been confirmed to be CO2 by CRISM analysis and have been hypothesised to come from adiabatic expansion and related to cooling of CO2 vents (Titus et al., 2007). Another mechanism leading to similar results, proposes that when the pressure is locally raised the equilibrium vapour pressure is exceeded for the ambient temperature and condensation occurs (Thomas et al., 2010). Attempts to model such processes quantitatively have shown that the dust drag on the gas is needed to reach supersaturation and condensation (Thomas et al., 2011a). Alternatively, Pommerol et al. (2011) noticed that the bright haloes all seem to originate from previous depositions of dark dust at the surface. They hypothesise that the bright haloes are caused by the sinking of the dust deposits into the ice.

Martínez et al. (2012) used atmospheric corrected HiRISE colour products, showing that dark spots located in Richardson crater present three distinct areas: dark core, bright halo and an intermediate area optically separating the core from the halo. Data from 1) dust optical depths derived from THEMIS, 2) CRISM detection of either CO_2 or H_2O ices, 3) surface pressure and temperature from TES and 4) numerical modelling were used. The results support the gas venting hypothesis and are consistent with temporal evolution of surface albedo.

The Kieffer model was backed up by computational fluid dynamic modelling (Thomas et al., 2011a), explaining several aspects of deposits on the polar surface, and the bright haloes surrounding dark spots and fans. Particle trajectories and deposition patterns linked to local wind and topography have been studied using various inputs for surface slopes, wind speeds, particles size distribution and mass loading. The computed jet models comply with observations and the Kieffer theory.

Experimental studies have looked at aspects of the formation of araneiform (de Villiers et al., 2012; Mc Keown et al., 2017, 2021) and cold jets (Kaufmann and Hagermann, 2017), adding confidence to the Kieffer model.

Active jets have not been observed yet. Only their deposits have been imaged which has led to the hypothesis that they could be active at very early local solar time in springtime, when the very first rays of sunlight hit the frozen surface of the ice. Alternatively, the optical depth of the jets may be too small to be detected against the background provided by the illuminated surface (Hansen et al., 2019, 2020). Additionally, other models have proposed that spots could be associated with low intensity venting of the majority of the excess basal pressure (Thomas et al., 2011a).

1.2. The Colour and Stereo Surface Imaging System

The Colour and Stereo Surface Imaging System (CaSSIS) onboard ExoMars Trace Gas Orbiter (Thomas et al., 2017) began its primary science phase in April 2018. Limited by the satellite's orbit inclination, high-latitude targets were first restricted to a maximum latitude of 74°, which was increased to 75° following a spacecraft manoeuvre in 2021. The reachable circum-polar region provides plenty of interesting targets, related to the processes described above. The orbit is approximately resonant with a frequency of roughly 30 days, which is useful for repeating observations and hence studying the temporal evolution of the surface. Repeated observations are beneficial for studying the morphologic and photometric evolution of features and have been acquired on an irregular basis. Previous observations of sublimation activity (spots, fans and spiders) close to the poles by other instruments such as HiRISE, CRISM or CTX (Mangold et al., 2004; Mangold, 2005; Hansen et al., 2010; Pilorget et al., 2011; Pommerol et al., 2011; Portyankina et al., 2012, 2017; Hao et al., 2019, 2020) have motivated the search for similar features within CaSSIS images. The key advantages of CaSSIS, in comparison with other imagers, are its high sensitivity (high signal-to-noise) in the panchromatic filter, possibility to image in 4 colour bands and its nearly simultaneous (40 s apart) stereo capability.

Thomas et al. (2017) detail the technical capabilities of CaSSIS such as providing images at 4.5m/pixel resolution combined with a moderate areal coverage (9 km × 40 km) up to four filters (NIR, RED, PAN and BLU, noted as N, R, P and B respectively). The original orbit of the TGO spacecraft also offers more variability in time of day and seasonality than the other cameras and spectrometers orbiting Mars. The BLU filter (centered at 497.4 nm) provides very high sensitivity to ice/frost and clouds. Surface and atmospheric processes can be best studied by using filter combinations including this filter (Thomas et al., 2017; Tornabene et al., 2018).

The main objectives of this work are to further test the Kieffer model as the general framework to explain Spring observations of the southern seasonal cap and refine various aspects of the physical processes affecting the surface at high latitude in Spring. We have searched through the catalogue of CaSSIS southern spring acquisitions to identify and analyse a selection of particularly interesting images.

To date (April 2021), CaSSIS has successfully acquired 22829 images with 3.3% of this database (i.e. 747 images) obtained during the first southern spring imaged at latitudes higher than 50°S. A variety of spot structures has been observed. Morphologies are studied through the high SNR in PAN and the colours inform on composition. Fig. 2 proposes a classification of the different dune spots observed throughout southern spring ($180° < L_S < 270°$) and a few images slightly before winter solstice and at the beginning of summer. The related sketches of the structures seen in this study are presented in Fig. 3. The nomenclature is as follow: A) Dark spot, B) Bright haloed spot, C) Ringed spot, D) Inverted spot, E) Dark haloed spot, F) Banded spot and G) Bright spot.

2. Methods and datasets

2.1. Study regions and image datasets

The study regions have been determined by the available coverage in the CaSSIS database and the diversity of morphologies observed in those regions. Fig. 1 shows a basemap of THEMIS-Day IR combined with MOLA, with each region labelled and Table 1 summarizes the information about each study area. All images presented here can be separated into two categories: **Dune spots** and **Araneiform Terrain**.

2.1.1. Dune spots

Tribal Mask Dune (TMD), Jeans Crater, East Mellish, Frosty Dune and Burroughs Crater all show spots appearing on top of isolated dunes or dune fields. The variety of spots seen throughout the available images, sometimes even within a single image, provides an interesting overview and helps establishing an enhanced formation mechanism.

Figs. S1 and S2, in supplementary material, provide mosaics of CaSSIS images for TMD and Jeans regions, respectively, using a MOLA-THEMIS (IR-Day) blend basemap.

2.1.2. Araneiform terrain

Hummingbird region, located west of Richardson Crater and North of the Mars Polar Lander [73°S, 169°E], is the only area presented in this study where araneiform terrain is visible. The spidery terrain seems to be following the edge of a regional flow-like, layered feature. Two locations within this area have been imaged and are shown by the two rectangles in Fig. 1. They are showing possible evidence of jet activity with atmospheric features possibly related to traces of activity at the surface.

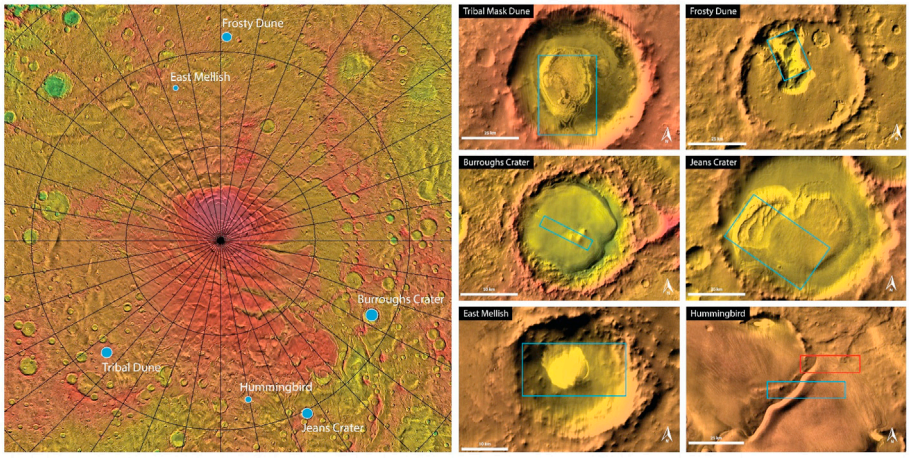

Fig. 1. (Left) Areas of interest (blue circles) over a THEMIS-Day IR combined with MOLA basemap (from JMARS) of the Martian south pole. (Right) Basemap of the six areas of interest. Polygons show the general location of CaSSIS footprint of images within the areas of interest. The naming of these areas is informal apart from the official Craters (Jeans and Burroughs).

Table 1
Study sites specifications and characteristics of the images presented. * Index column refers to Fig. 2 tile indexes. ** Informal names.

Study Site	Latitude	Longitude	MOLA Elevation	Acquisition ID	LST	Ls	Sol #	Incidence	Phase	Emission	Filters	Index*
Tribal Mask Dune (TMD)**	73°S	223°E	1000m	MY34_002252_273_0	09:53:05	182.16	375	75.157	82.564	11.147	NIR-PAN-BLU	E
				MY34_002301_267_0	07:31:59	184.44	379	81.746	90.978	11.234	NIR-RED-PAN-BLU	F
				MY34_002401_271_1	06:43:27	189.15	387	83.241	94.382	11.234	NIR-RED-PAN	H
				MY34_002401_271_2	06:42:37	189.15	387	83.297	72.321	11.034	RED-PAN-BLU	(H)
				MY34_002451_274_1	06:19:22	191.52	391	83.946	95.157	11.281	NIR-RED-PAN	I
				MY34_002451_274_2	06:18:34	191.52	391	84.003	73.139	10.986	NIR-PAN-BLU	(I)
				MY34_003545_273_0	09:03:21	246.54	478	55.891	65.358	11.17	NIR-PAN-BLU	O
				MY35_011080_276_0	17:06:56	202.97	410	77.086	70.196	10.881	NIR-RED-PAN-BLU	J
				MY35_011812_263_0	00:43:55	240.07	468	84.751	81.314	11.082	NIR-PAN-BLU	M
Jeans Crater	69°S	153°E	850m	MY34_002141_258_0	08:50:51	177.05	367	77.662	80.033	11.256	NIR-RED-PAN-BLU	C
				MY34_002228_258_1	07:11:57	181.05	373	83.428	89.979	11.301	NIR-PAN-BLU	D
				MY34_002228_258_2	07:11:53	181.05	373	83.412	77.112	10.951	RED-PAN-BLU	(D)
				MY34_003347_258_0	09:57:41	236.28	463	52.425	53.143	11.577	NIR-RED-PAN-BLU	L
				MY35_011195_283_0	16:22:47	208.65	419	70.817	69.305	10.791		K

(*continued on next page*)

Table 1 (*continued*)

Study Site	Latitude	Longitude	MOLA Elevation	Acquisition ID	LST	Ls	Sol #	Incidence	Phase	Emission	Filters	Index*
											NIR-PAN-BLU	
				MY35_012100_258_0	18:31:12	255.03	491	69.964	70.45	10.885	NIR-PAN-BLU	P
				MY35_012473_258_0	11:34:33	274.31	521	44.867	46.117	11.819	NIR-PAN-BLU	Q
Hummingbird**	73°S	169°E	1700m	MY34_002365_266_1	06:13:05	187.45	384	86.03	96.791	11.271	NIR-RED-PAN	
				MY34_002365_266_2	06:12:33	187.45	384	86.068	75.524	10.984	RED-PAN-BLU	
				MY34_003372_266_0	10:50:38	237.57	465	52.915	54.264	11.266	NIR-RED-PAN-BLU	
				MY34_003484_266_0	08:50:35	243.37	474	57.007	64.549	11.345	NIR-PAN-BLU	
				MY34_003485_275_0	10:48:46	243.43	474	51.787	58.783	11.242	NIR-PAN-BLU	
				MY34_004604_275_0	12:53:20	300.52	563	52.265	52.731	11.046	NIR-PAN-BLU	
				MY35_013780_276_0	15:52:57	337.04	625	72.137	67.016	10.959	NIR-PAN-BLU	
East Mellish**	73°S	343°E	850m	MY34_002073_266_1	11:38:24	173.96	361	75.922	74.282	11.162	RED-PAN-BLU	A
				MY34_002073_266_2	11:37:32	173.96	361	75.88	77.901	11.101	NIR-RED-PAN	(A)
				MY34_002359_267_1	06:20:35	187.16	384	85.61	96.271	11.271	NIR-RED-PAN	G
				MY34_002359_267_2	06:19:57	187.16	384	85.652	75.203	10.987	RED-PAN-BLU	(G)
Frosty Dune**	68°S	0.94°E	500m	MY34_003464_256_1	07:20:59	242.34	472	62.059	69.291	11.428	NIR-PAN-BLU	N
				MY34_003464_256_2	07:22:13	242.34	472	61.95	55.69	10.84	RED-PAN-BLU	(N)
				MY35_012565_255_0	09:19:09	279.01	528	49.693	49.174	11.143	NIR-PAN-BLU	R
Burroughs Crater	72°S	117°E	400m	MY34_002093_264_0	10:40:49	174.86	363	75.63	75.2	11.176	NIR-RED-PAN-BLU	B

2.2. Classification of spots

The goal of this study is to test and refine the model proposed for the formation and evolution of spots using CaSSIS data. For this purpose, all images with identified spots have been sorted with respect to L_S values in Fig. 2. Each tile letter correspond to the index column in Table 1. Fig. 3 shows a simplified version of all morphologies of spots observed in this study, with an associated CaSSIS example image.

2.3. Image acquisition and data extraction

A total of 2522 images (as per April 2021) have been acquired at latitudes higher than 50°S and within a solar longitude (L_S) range of 180–270° corresponding to the southern spring season. This represents 11% of the complete database to date. The process of capturing images of the surface with CaSSIS has been explained in details in Almeida et al. (this issue). Once acquired, the raw data images are reduced through

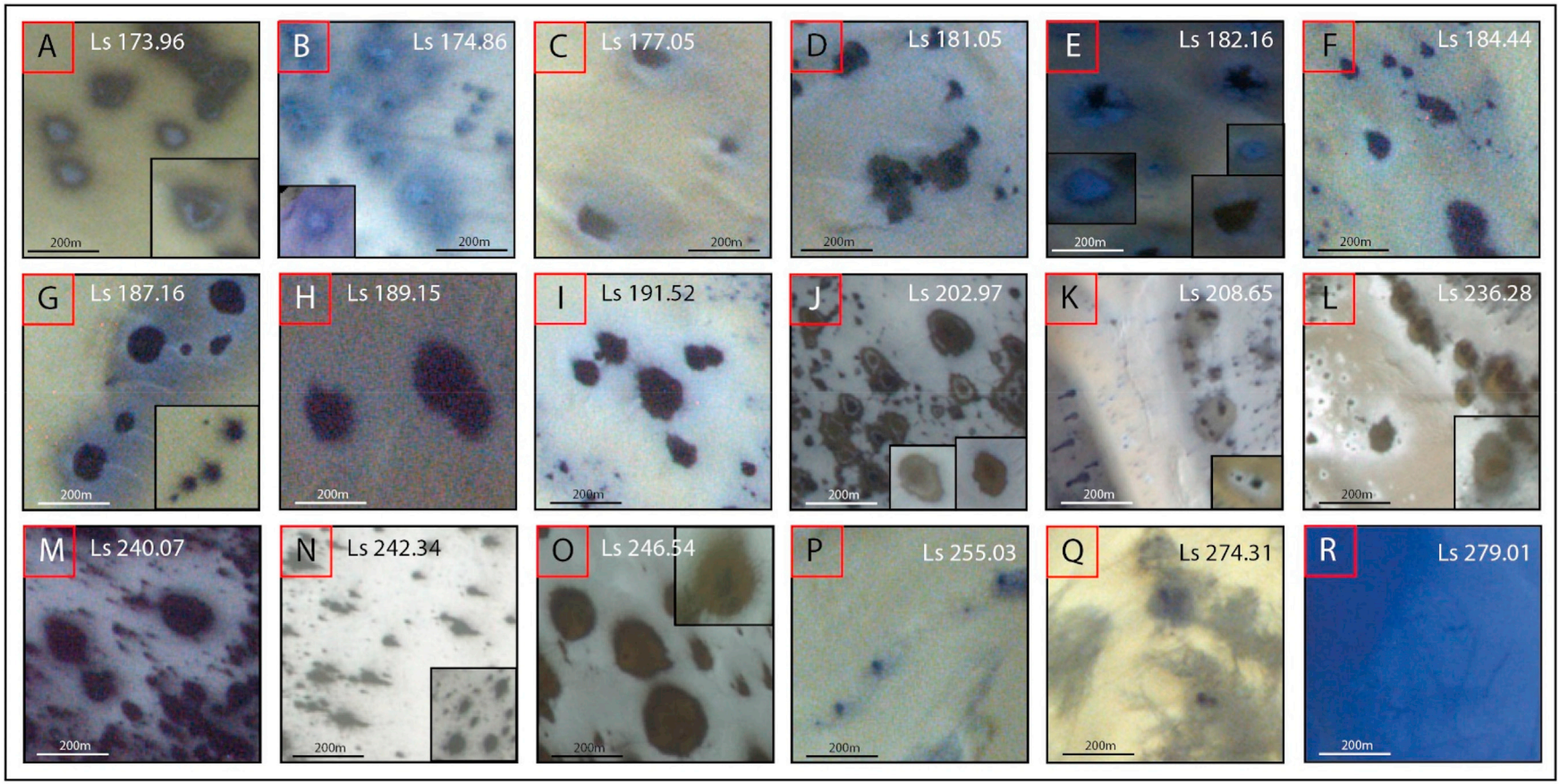

Fig. 2. Mosaic of spot samples seen in all images listed in Table 1 under the index column. Tiles A-C were acquired at the end of southern winter, D-P during southern spring and Q-R at the beginning of southern summer. Fig. 3 proposes a schematization of all structures of spot example observed in this study.

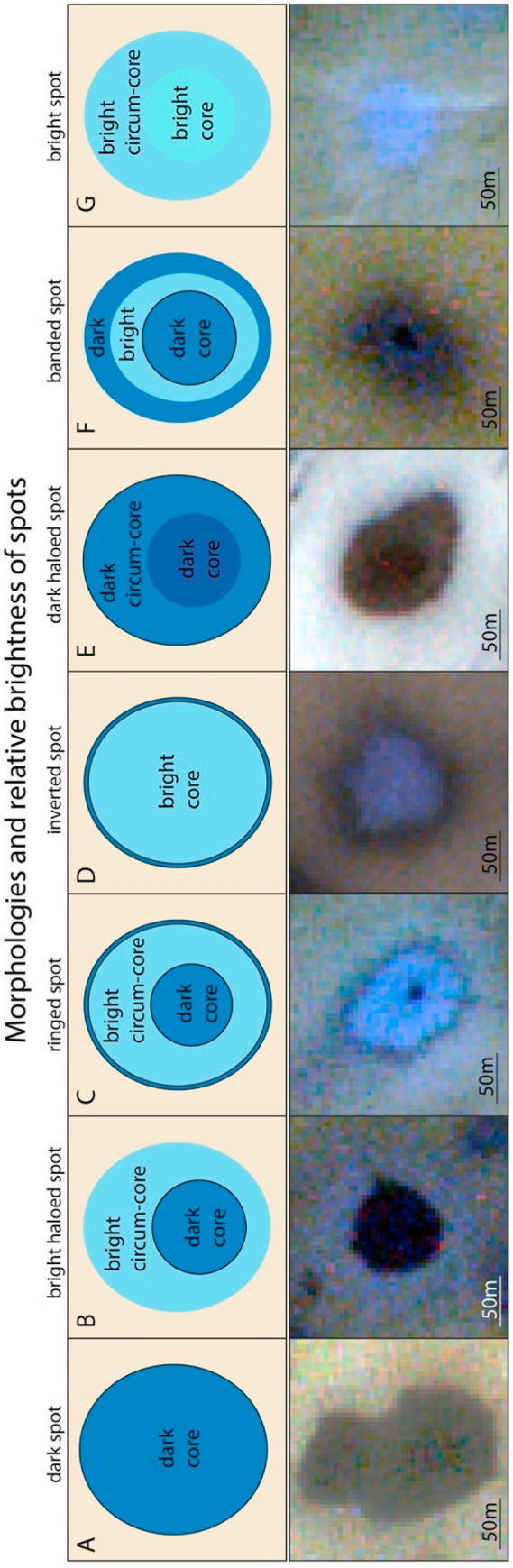

Fig. 3. Sketches of spot structures (top row) and example CaSSIS images (bottom row) seen during the southern spring. Dark blue and purple colours in the sketches indicate relatively dark deposits in comparison to the bright deposits (bright blues). The solid black line indicates a strong and sharp contrast between two parts of a structure.

calibration pipelines. Pommerol et al. (this issue) and Perry et al. (this issue) explain thoroughly the radiometric and geometric calibrations, respectively. The final products are stored as ISIS.cub files containing data in all available filters. They are then read into the ENVI™ image analysis software. Regions of interest (ROI) have been defined in each image. The images are calibrated to units of radiance factor ("I over F"). I/F, intensity/flux, is defined as the ratio of the observed radiance to the radiance of a 100% lambertian reflector with the sun and camera orthogonal to the observing surface.

The extracted ROIs are used to compute average reflectance, brightness and band ratio comparisons presented in Section 3. For each ROI, a large number of pixel have been used to increase the signal-to-noise. For backgrounds and large homogeneous areas (dunes in summer), the number of pixels ranges between 10 000 and 160 000. Because of the smaller size of the features, only 250 to 17000 pixels can be averaged for spots, rings and haloes. The definition of the ROIs to select homogeneous regions is also quite challenging. The standard deviations for these regions range between 0.4% and 0.03%.

The radiance factor depends on the local illumination conditions (solar incidence, phase and emission angles). To obtain the reflectance factor, the I/F values extracted from the radiometrically calibrated images need to be divided by the cosine of the incidence angle, this reflectance factor definition uses a global incidence angle value for the entire scene and therefore ignores local topographic variations. Thomas et al. (this issue) explain that the sensitivity of CaSSIS is slightly less than predicted (86.9% of the expected value), and the correction factors of Thomas et al. (this issue) have been applied here to mitigate this effect.

The relative brightness ratio compares the reflectance of a dark area (i.e. dark core or dark ring) with a closeby bright area (usually the surrounding background terrain). This technique is widely used in Martian planetary photometry studies (Daubar et al., 2016; Schaefer et al., 2019; Munaretto et al., 2020, 2021, 2022) and allows to better compare the photometric properties of surface features imaged under different illumination and observation conditions without the need to assume any particular bidirectional reflectance distribution function (usually the Lambert one) for the surface that is implied for absolute photometry. Relative brightness ratios are then compared between various images to determine the evolution of the relative brightness over a period of time. We also made use of the Colour Band Ratio Composite (CBRC), explained in Tornabene et al. (2018). The ICE/ATM CRBC product uses a specific set of ratios to help differentiating between ice/atmospheric features and dusty surface materials.

From TES and THEMIS nadir observations, and estimates from MCS limb observations, column dust optical depth (CDOD) have been spatially interpolated for Martian Year 34 (Montabone et al., 2020), despite the Planet-Encircling Dust Event (PEDE), using a kriging method - a linear least square type interpolation minimising the error variance by weighting each data point (Journel and Huijbregts, 1976; Montabone et al., 2015). The averaged IR absorption (9.3 μm) CDOD normalized at 610Pa for MY34 shows a maximum value of 0.525 during Ls 215–225° for latitudes higher than 70°S, however our dataset does not cover these solar longitudes and the maximum atmospheric dust opacity value reached is therefore 0.37 for this study.

The CaSSIS images in this study are presented without atmospheric correction, considering a low atmospheric opacity.

3. Results and interpretation

In this section, we present the spectrophotometric analysis comprising reflectance spectra, reflectance profiles, colour band ratios and brightness ratios.

3.1. Temporal evolution of spots

From the overview of different types of spots in Fig. 2 and the classification sketches in Fig. 3, a clear evolution can be observed. From

previous studies, only bright haloes and dark spots have been linked together in time. Bright, inverted, ringed and banded spots are an addition to this evolution model. We compute here the brightness ratios between dark and bright units, where dark units are defined as the dark spot cores or, for inverted spots, the dark ring surrounding the bright core. The bright units consist of bright cores or bright haloes. The background is defined as the closest neutral terrain from the spots and, when applicable, their haloes. The evolution of the brightness ratio of spots throughout southern spring can be followed in Fig. 4.

Fig. 4 top row shows the brightness ratio of dark features over the surrounding background, and comprises data from latitudes between 68°S and 73°S. However, we expect the sublimation processes to be highly dependent on latitude due to mean temperature variability, thus two additional graphs are shown for two latitude ranges in Fig. 4 bottom row. In particular, the bottom-left graph shows the portion of data within latitudes 72–73°S, while the bottom-right reports the measurements only from 68 to 69°S. The trend obtained from the entire dataset shows a curious behaviour. Around the spring equinox ($L_S = 180°$), the brightness ratio is at its maximum. It then decreases drastically up until $L_S = 200°$, then increases until $L_S = 255°$, with a minimum based on two observations around $L_S = 246°$. It decreases slowly with the arrival of summer solstice. The latitude range 68–69° has data spaced evenly across the timescale while the higher latitude range lacks data in mid-spring and at the end of spring.

The TMD area provides good information about recurring spots over time due to many overlapping images. Fig. 5 shows three images with sublimation spots. Image MY34_002252_273_0, in sub-panel A, taken in early spring (Ls 182.1° - Year 34 Sol 375), presents dark cores (blue polygons) associated with brighter haloes (orange polygons). These outlines have been pasted onto the two following images taken later in spring, L_S 246.54° (Year 34, Sol 478) and 240.07° (Year 35, Sol 468) respectively, to show a possible evolution of visual morphology.

In general, we can observe that spots recur at the same position in every Martian year (Thomas et al., 2010). However, the morphology varies from early spring to mid-spring and can be dissimilar the following year where new spots can emerge as well. The year lapse between Fig. 5 panels B and C shows the extent of the recurring in position as well as the individualisation of a new spot - that was most likely concealed by the cluster of small-sized depositions early on. The outer haloes seen in Fig. 5A are reflected in Fig. 6 by a soft slope in the reflectance profiles. The brighter haloes cause a slight increase before reaching the minimum at the core of spots. Mid-spring spots, without bright haloes have a strong reflectance drop. The NIR and PAN filters, have a curious behaviour where there is a slight reflectance bump at the spot's centre. This characteristic is not visible in image MY35_011812_263_0 probably because of a low signal to noise.

Two additional sets of spots are shown in Fig. 7. In the early-spring observation, the spots exhibit bright deposits within darker features that later fade out and make the spots appear as dark uniform features. The first showcase consists of two bright spots and a surrounding bright halo with no apparent dark core transitioning into a dark feature merging both bright features. In the second showcase, we can see a three-layer feature with a dark core, transient bright halo and secondary dark halo. This layering disappears, as before, into a single dark feature. It appears that the boundary of the structure is not correlating with one of the preceding layer outlines but in between the outer and middle layers. The profiles in this case, show a different behaviour with the background having the same reflectance factor in both images, the dark spot showing

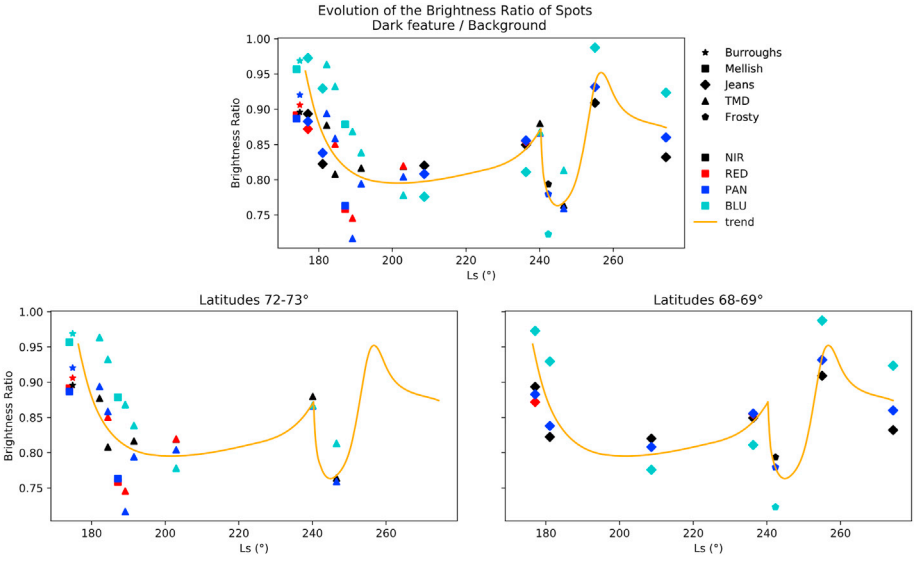

Fig. 4. Average brightness ratio for each acquisition in Fig. 2 as a function of time in L_S values. (Top) Dark features ratio with neighbouring background. Dark features here are assigned to dark spots and cores. (Bottom) Average brightness ratio for images within latitudes of 72–73°S (left) and within latitudes of 68–69°S (right). Uncertainties are relatively small and negligible and this is explained by the fact that homogeneous data have been chosen for each ROI type, and a large number of pixels are used for all data points.

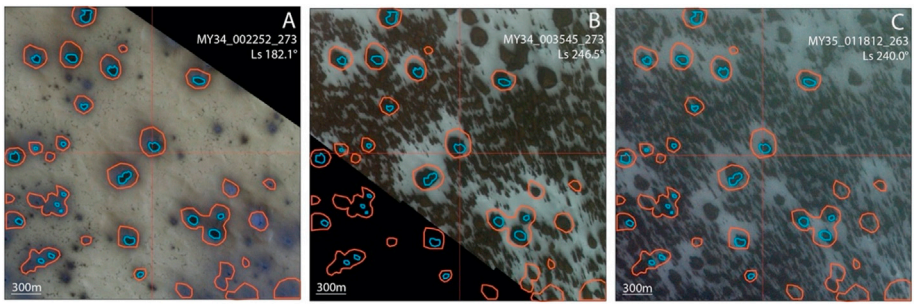

Fig. 5. Time evolution of dune spots in an unnamed crater situated South of Stoney Crater. Spring image (A) and summer images (B and C) are shown with the NPB filter combination and north up. Blue and orange polygons delimit the structures of spots with a dark core and a bright halo, as seen in A.

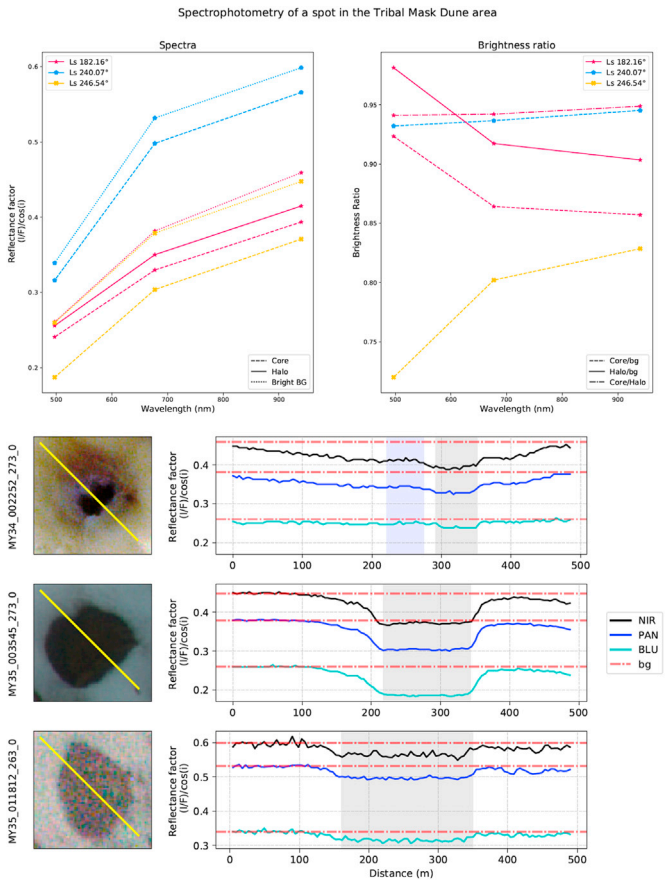

Fig. 6. (Top) Spectral plot of spots, halos and bright background of three features in the Tribal Mask Region presented in Fig. 5. (Bottom) Profiles of the reflectance factor. Profiles are oriented with respect to the corresponding image, NW to SE and are slightly extended from the current sub-images view to the NW.

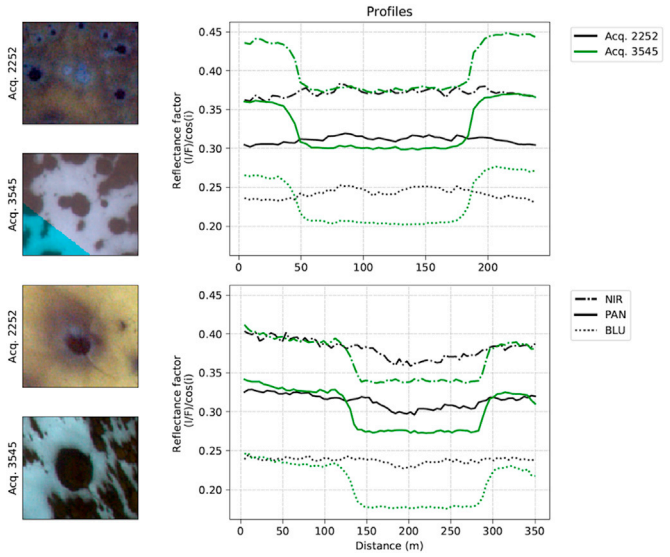

Fig. 7. Seasonal evolution of two sets of features from images MY34_002252_273_0 (L_S 182.1°) and MY34_003545_273_0 (L_S 246.5°). The profiles of the latter image show strong drop in reflectance factor while bright spots in the earlier image show less variation.

a clear drop in reflectance in all filters, and the layered spot has two bumps associated with the brighter deposits surrounding the dark core.

As the physical evolution of spots through spring is made obvious by overlapping images, the spectral analysis showed a strong correlation between early inverted spots, early bright haloes and late dark spots.

Fig. 8 (A, B and C) shows spectral plots and brightness ratio with the surrounding background for each of the three structures. We mainly observe a shift in the spectral responses, which supports a common physical origin.

3.2. Seasonal comparison

Frosty Dune: This area, located in Sisyphi Planum, shows a pitted crater with a central dark sand dune and gullies on the edge of the pit. The three images covering the dune were taken in mid-spring (two from a stereo pair) and early summer, respectively (see Table 1). Fig. 9 A & A1 shows that the dune is covered by frost and dark spots, creating a high contrast with the surrounding terrains in late spring. Free of ice in summer (Fig. 9 B & B1), the dune exhibits a smooth dark sand cover, again in contrast with the bright neighbouring terrains. Relative reflectance profiles are shown in Fig. 10 along a sketch of the area. While the spring image was taken at a time where regionally the CO_2 ice layer would have completely sublimated, the dune is still covered by frost. The spectra in Fig. 11 show that the terrain used as a background value (Plateau floor) is slightly brighter in the spring image which could indicate that a thin layer of ice is still remaining. The reflectance profiles show the distribution of spots on the frosty dune and an overall brighter surface than the defined background. In Summer, the dune itself is covered by dark basaltic sand with a low reflectance factor, lower than the defined background (Plateau floor) and the surrounding pit floor.

Additionally, the summer image is presented in Fig. 9 with a 2% linear stretch making the dune globally dark. In supplementary material, Fig. S 3 shows a Gaussian stretch applied at different locations within the image (red stars), allowing a better visualisation of darker and brighter areas within the dune.

East Mellish: This area is similarly covered by two stereo pairs, Fig. 12 shows the mound at L_S 174° (first stereo acquisition) and at L_S 187°, with each time a RPB filter combination. The reflectance profiles are shown in Fig. 13 (A and B). The profiles were defined going through areas with spots, and crossing over the bright middle plateau (see Fig. 12 for the profile line). Stereo acquisition MY34_002073_266 (L_S 173.96°) was taken right before the spring equinox. The surface has a quasi-constant reflectance factor in the bright areas and shows a clear positioning of dark spots by the dips in all filters. There is a slight increase in the slope in the centre mound. Bright haloes and dark spots share, as seen previously, a similar trend with a shift in value, only the background shows a redder slope (steeper slope from BLU to PAN wavelengths, 497 nm and 677 nm respectively) .

The short time evolution of the mound activity is shown in Fig. 12 and we focus on the appearance of individual spots. From Fig. 3, categories C (ringed spot) and D (inverted spot) are visible in the first stereo pair, and then shift to categories A (dark spot) and B (bright haloed spot) in the second pair. The edge of the mound - where topographic contrast is stronger - first shows activity in image MY34_002073_266_1. It is thought that all spots in this image are ringed to some extent, and have simply a lower contrast or are more difficult to delimit with the actual signal-to-noise ratio and resolution. A few clear inverted and ringed spots are visible and pointed out by the red squares in Fig. 12. Unusual spots (ringed and inverted) have disappeared in image MY34_002359_267_2 and only a dark core with a brighter halo are remaining at the edge of the mound. The activity in the central part, hence being more recent, appears to be mainly composed of a dark spot with or without a small halo. A small cloud is noticeable in the image MY34_002073_266_1, this was achieved by a colour combination using the BLU filter. Although the second stereo pair did not feature an optimal colour combination, the cloud is observable through the PAN filter and is showed in more detail in the Results section Fig. 17.

Hummingbird: This region, with araneiform terrains, is showing high colour contrast and can be followed in time through various

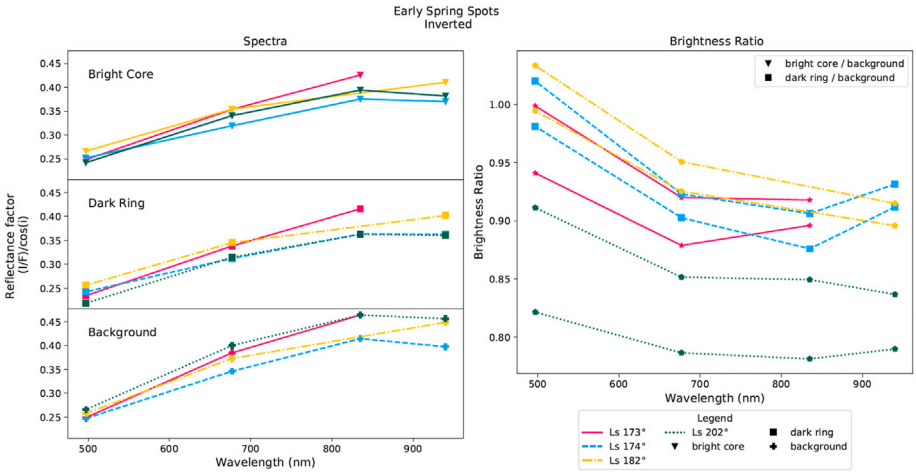

Fig. 8.A. Comparative spectrophotometry of early spots (inverted). Left panels are the respective spectral plots and the right panel shows the brightness ratios with the background ROI.

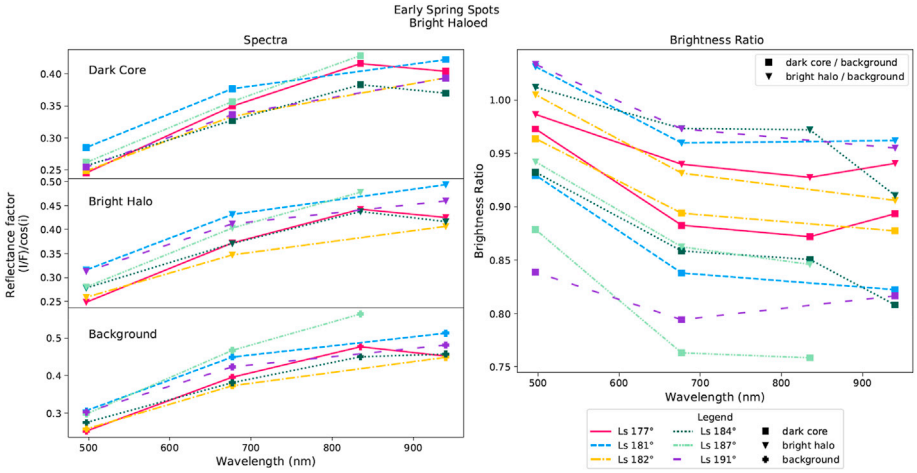

Fig. 8.B. Comparative spectrophotometry of early spots (haloed). Left panels are the respective spectral plots and the right panel shows the brightness ratios with the background ROI.

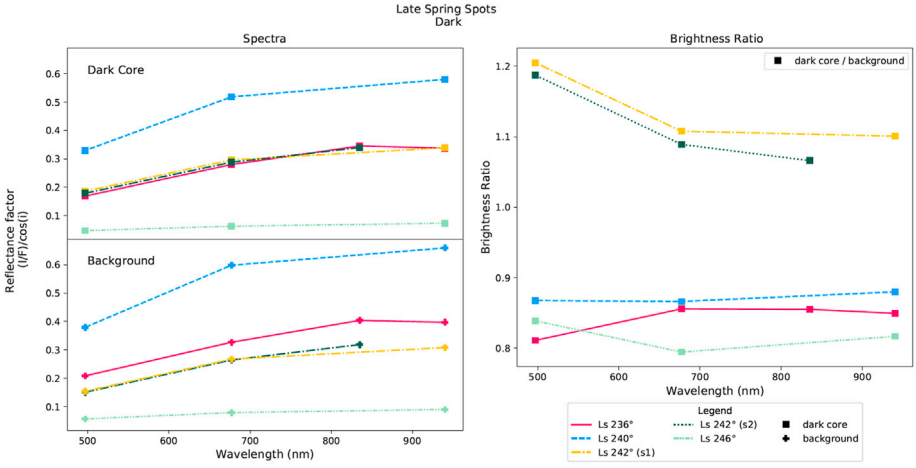

Fig. 8.C. Comparative spectrophotometry of late spots (dark). Left panels are the respective spectral plots and the right panel shows the brightness ratios with the background ROI.

acquisitions. Several images have shown distinctive elongated araneiforms likely linked to jet activity. Fig. 14 shows various sub-terrain with more or less wide channels (araneiform troughs). The variability in size is thought to be evidence of erosion from past or recent activity. Thinner

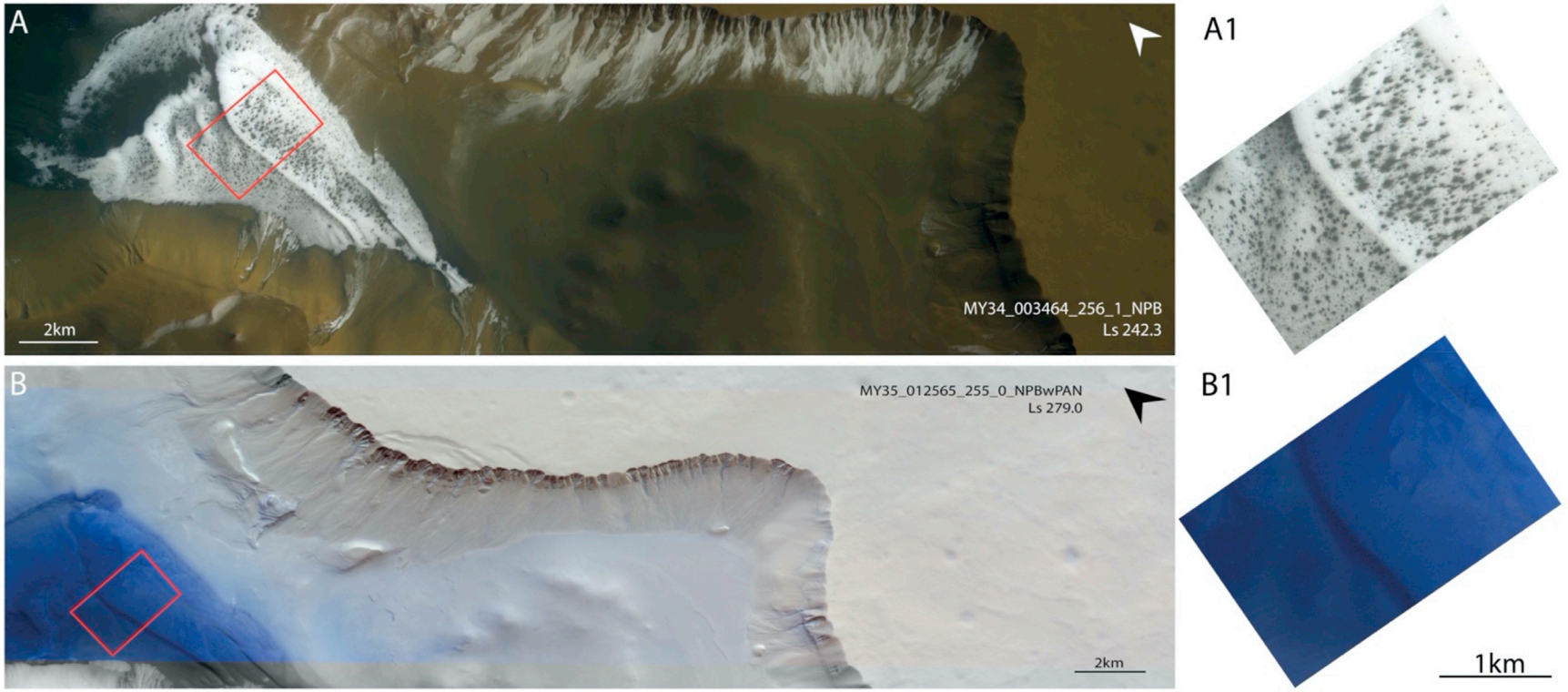

Fig. 9. The gullied pit crater dune in Sisyphi Planum is located at a longitude of 0.94°E and latitude of 68.2°S. (A) Image MY34_003464_256 (stereo pair available) was taken in mid-spring (Ls 242.3°, incidence 62.1° and LST 07:20:59) where the dune is still covered by frost and apparent variously shaped spots. (B) Image MY35_012565_255_0 taken in early summertime. The dune is free from ice, showing a smooth dark sand surface (blue in the NPB composite) in contrast to the bright surrounding. (A1 & B1) Zoom on the dune crest.

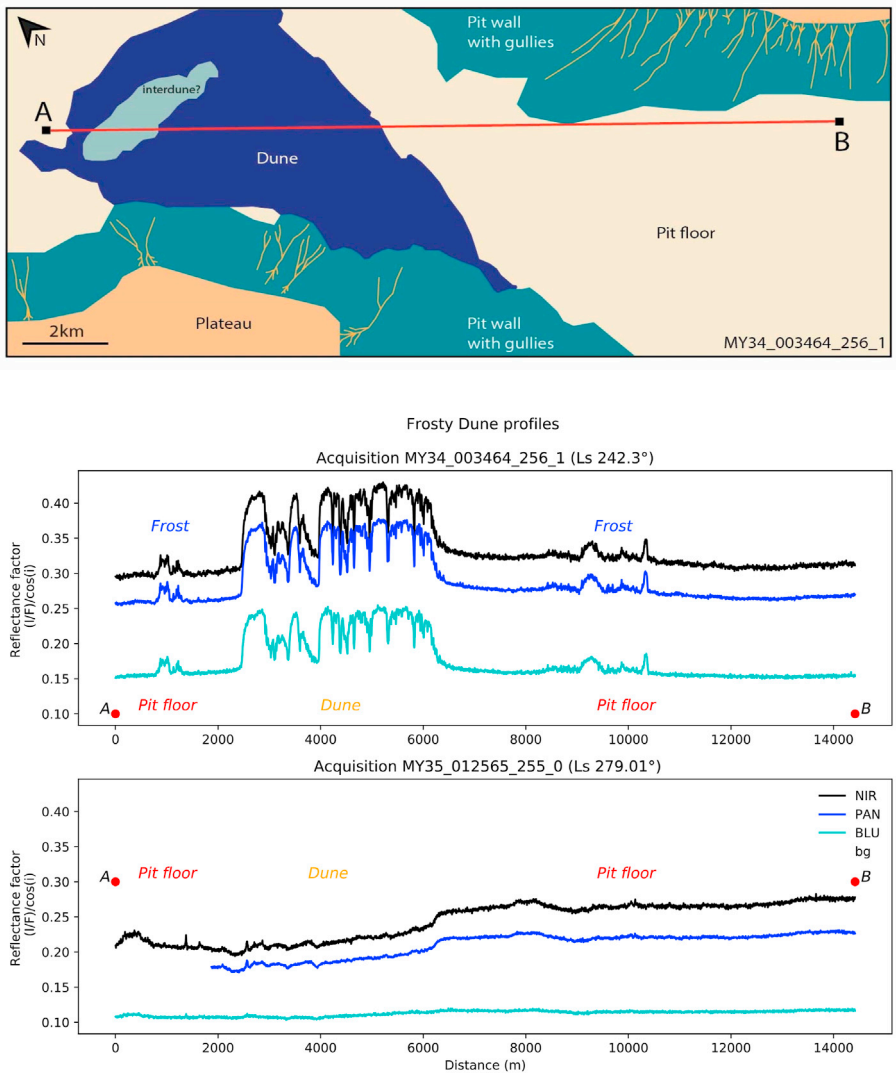

Fig. 10. (Top) Sketch view of image MY34_003464_256_1. The red line represents the transect profile position for both images. (Middle) Spatial profile of the reflectance factor for image MY34_003464_256_1 when frost and spots are covering a portion the surface. (Bottom) Spatial profile of the reflectance factor for image MY35_012565_255_0 when the dune is free of ice and the dark sand produced a strong contrast with the surrounding environment.

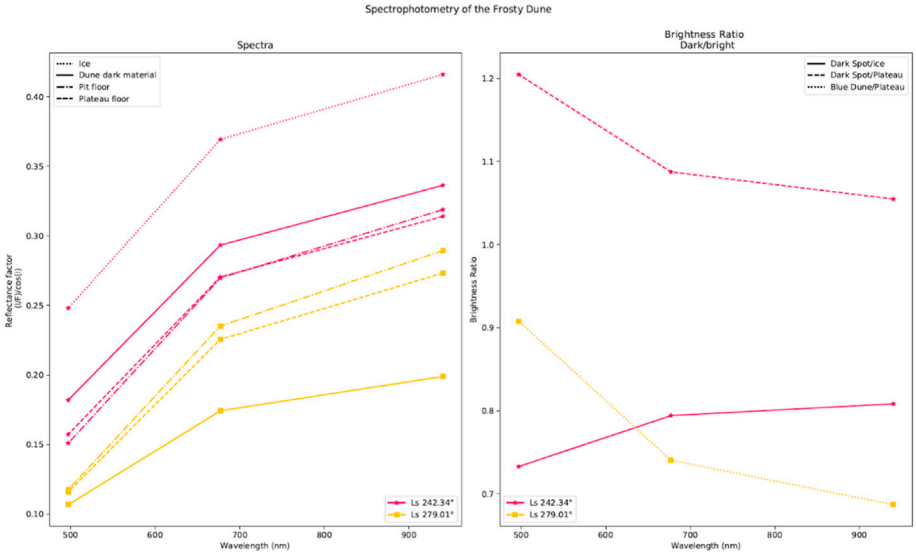

Fig. 11. Spectrophotometry of the Frosty dune region. (Left) Spectral plots for defined ROIs. (Right) Brightness ratio of ROIs with the surrounding backgrounds.

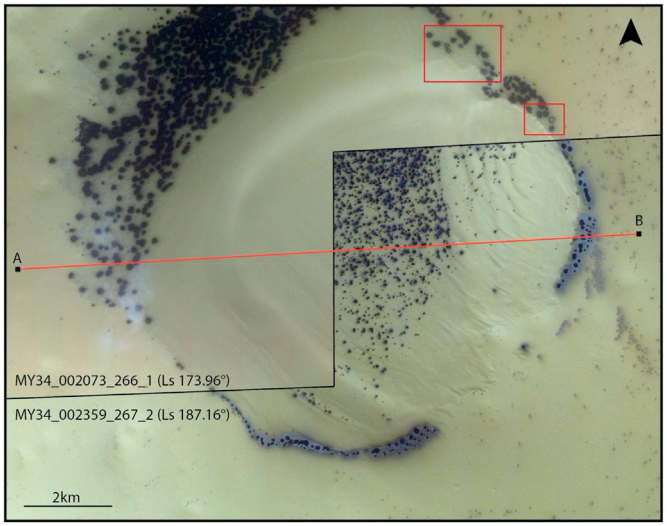

Fig. 12. Overlapping images of MY34_002073_266_1 (L_S 173.96°) and MY34_002359_267_2 (L_S 187.16°) in RED-PAN-BLU colour combinations. The red squares delimit area where ringed spots are clearly visible. The red line is the profile section shown in Fig. 13A.

troughs appear here with dark material in the vicinity, which is coherent with active processes (Piqueux et al., 2003). Wider troughs do not show presence of dark material and this could be explained by a lower topographic contrast not affected as much by the basal sublimation processes of the CO_2 ice layer.

Images of this spidery terrain are available at the beginning of spring and mid/end-season. In Fig. 14, four sub-units (and two intermediates units) have been identified from the number of erosion marks, spider troughs and by colour variations. Sub-image A, using a NRP colour combination, appears greyscale with little colour diversity. Texture and contrast are still clearly discernible, according to the L_S the surface is covered by a CO_2 layer. Sub-image B, taken later in spring, shows more diversity on the bare surface. Terrain a1 lacks erosion marks and appears to be of a lighter colour. Terrain a2 is showing wide erosion channels with no dark deposits in the vicinity. Terrain a3 is presenting the most activity for both images, the spider troughs are thinner and many spider cores are visible. In early springtime, small patches of dark material rest on top of thin spider cores. Intermediate terrains named a3t and a3/4 share visual similarities with both terrains a3 and a4 or seem to be a transitional zone between these terrains. When the surface is free of ice, in acquisition MY34_003484_266_0, colour contrast between young araneiform terrains and areas with little to no troughs is much more discernible than in image MY34_002365_266_1.

The second area of interest is outlined by the red polygon in Fig. 1. We follow a curious surface pattern through seasons resembling a hummingbird, hence the informal nickname used for this area.

In Fig. 15 (see Supplementary Fig. S4 for full size), sub-images A and B were acquired with the same filters (NPB) and yet they appear completely different. The illumination conditions are similar with the incidence angle around 52°, local solar time of 10:49 and a solar longitude difference of only of 6°. Sub-image A appears cloudy in regions where the terrain seems covered by spidery terrain, the blue toned atmospheric feature overshadows a large portion of the surface which appears to be a dark terrain with a bright surrounding area. Sub-image B, taken slightly later, shows again the bright background terrain and a dark brown terrain. Summer images C and D, despite an optimal colour combination, have no colour diversity and show only contrasts between dark (full of spiders) and bright areas. The two summer images are also presented here with the same filter combination but have different illumination conditions. Separated by a Martian year, the differences are not striking. The darker terrain featured in sub-figures A and B are also optically darker during summertime. From the spectral data in Fig. 16, only image MY34_003372_266_0, with the clouds shadowing the surface, shows a distinctive ratio in the BLU filter.

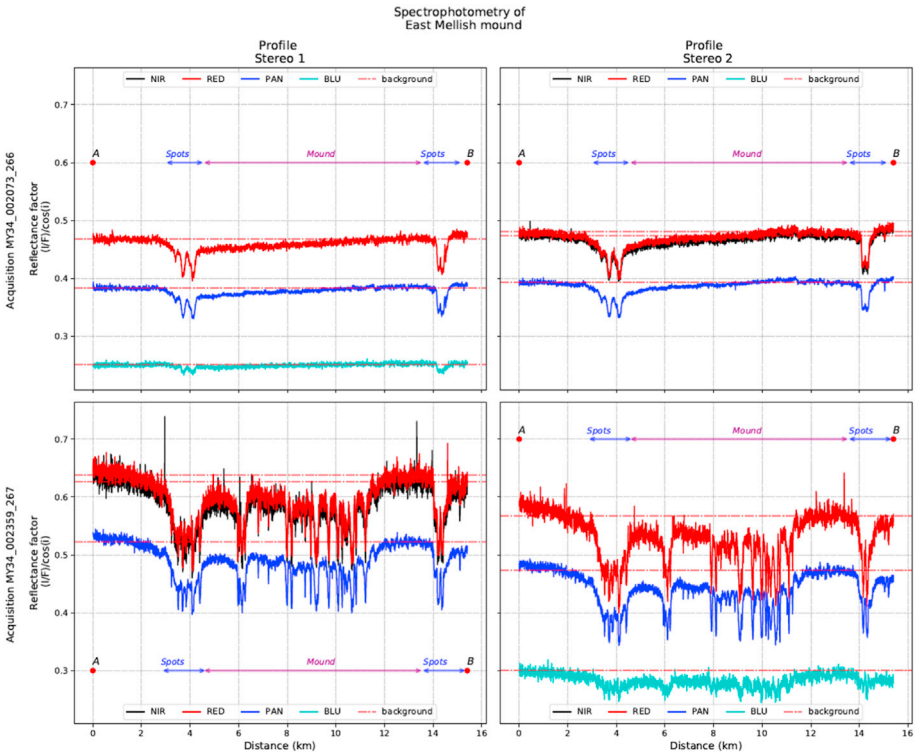

Fig. 13.A. Profiles for the image of the East Mellish mound. The profile is shown in Fig. 12 by the red line.

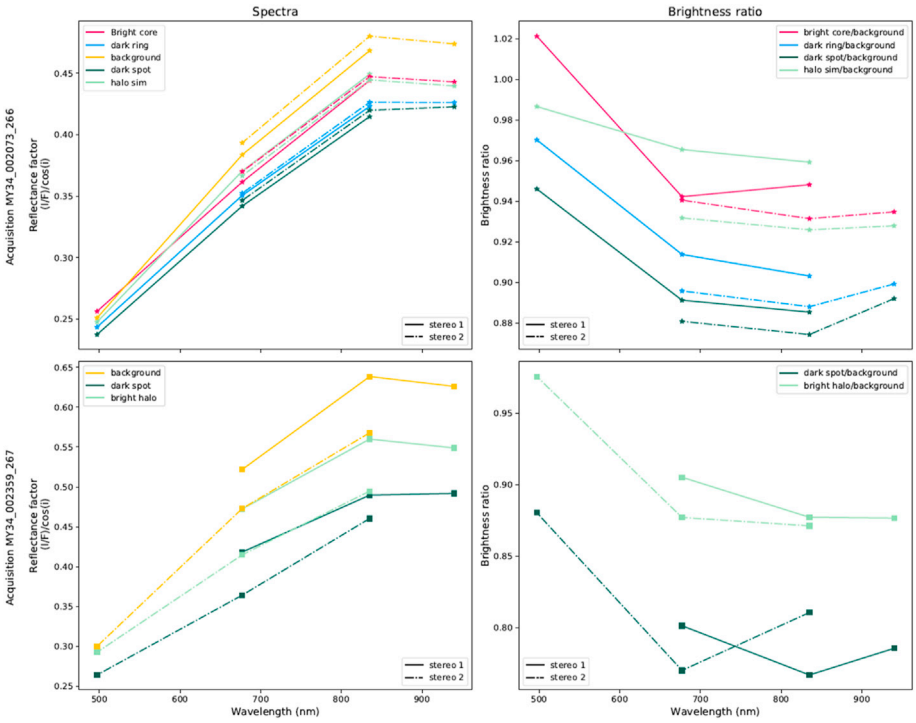

Fig. 13.B. Spectrophotometry for the image of the East Mellish mound (Fig. 12).

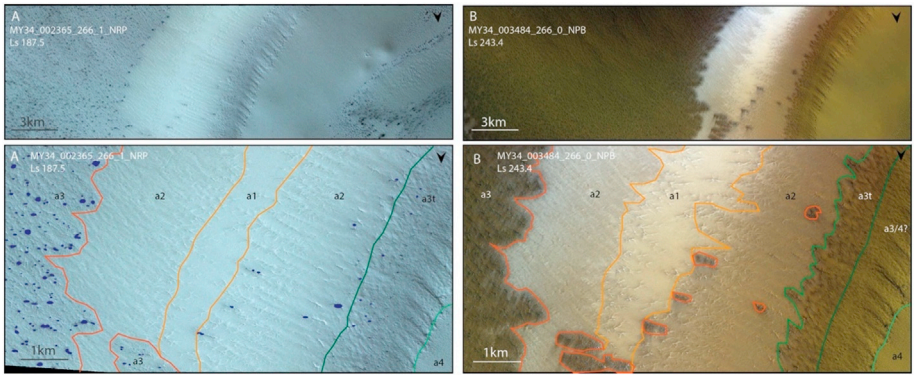

Fig. 14. Reference zone of the blue polygon in the Hummingbird region sub-image from Fig. 1. (Left) Image MY34_002365_266_1 taken in early spring (L_S 187.5°). (Right) Image MY34_003484_266_0 taken around the perihelion (L_S 243.4°). Different zones are annotated from a1 to a4, with respect to visible activity and young spider abundance.

3.3. Diffuse atmospheric features

Diffuse atmospheric features have been observed in the East Mellish, Burroughs and Hummingbird regions, and are thought to be linked with activity from the surface as they correlate with unusual spots and spider fields. Stereo acquisitions are highly beneficial for momentary processes and allow observation of dynamic features such as clouds.

East Mellish: Fig. 17 shows the stereo pair MY34_002073_266 where a diffuse feature is seen moving when comparing both images.

Although this feature was clearly visible in the stereo #1 (Fig. 17 A) which includes the BLU filter, the second stereo was acquired without, making it difficult to locate precisely the same feature. Fortunately, the diffuse feature is also seen in the PAN filter, albeit with a reduced contrast. Fig. 17 A_PAN & B_PAN are individual PAN images with the feature delimited by the green and blue polygons for stereo #1 and #2, respectively. By stretching the image with a Gaussian stretch, we enhanced the visualisation of the diffuse cloud and calculated a movement speed. By first estimating a direction of propagation, assuming a direct path from the location of the cloud in the first stereo to its final position in the second stereo, it is possible to extract the distance using the pixel resolution (usually around 4.49m/pixel). We propose two possible directions of propagation (Fig. 17 Cloud_1 & Cloud_2). The time between each stereo image is around 45 s, hence we can calculate speeds with possible speed ranges of 11–35 m/s and 17–30 m/s.

A second stereo pair, MY34_002359_267, was acquired later the same year at L_S 187.16°. Fig. 18 clearly shows the change in spots morphologies, going from inverted and ringed spots to bright-haloed spots. The diffuse feature visible in sub-panel A disappeared in sub-panel B.

Burroughs Crater: Fig. 19 shows the central region of Burroughs crater covered with many ringed spots and/or dark spots (categories A and C in Fig. 2). The contrast between parts of each spot structure is not always clear to establish. A cloudy feature is visible, which does not totally obscure the surface. Sub-image A shows a close up of spot morphologies deviating from the usual known dark spots, here labelled ringed spots. These appear with a dark core, an oriented bright deposit and a darker halo uniting them together into one feature. The edge of the

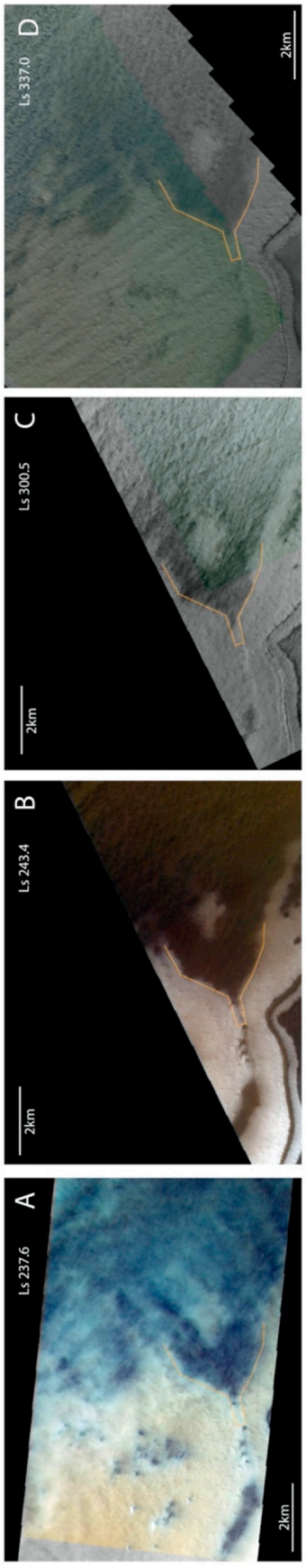

Fig. 15. CaSSIS sub-images of the Hummingbird pattern, with a colour combination using a NPB filters combination superposed onto the full greyscale PAN filter (C and D) to better see the overlap of the images. The yellow dashed line shows the edge of the dark pattern. South is up. (A) Image MY34_003372_266_0 at L_S 237.6° displays what appears to be clouds covering a major portion of the surface, which follows the edge of the darker underlying terrain. (B) Image MY34_003485_275_0 at L_S 243.4° (C) Image MY34_004604_275_0 at L_S 300.5° (D) Image MY35_013780_276_0 at L_S 337.0°.

atmospheric feature is visible thanks to the contrast with the similar bare surface in sub-image B. A peculiar spot (inverted spot), similarly seen in Fig. 12, is visible at the very edge of the image and no other similar spots have been found in the entire image.

Fig. 20 shows the spectra and the brightness ratio for Burroughs area. Bright halo and dark spots within the image, show similar spectral responses, the same way the dark ring and bright ring do. This once more follows the hypothesis that dark spots and bright haloes have the same physical origin.

Following Tornabene et al. (2018), Colour Band Ratio Composite (CBRC) can help distinguishing compositions onto the surface. Here we decided to use the Ice/Atmosphere (ICE/ATM-ALL) index to complement the analysis of the atmospheric feature seen on Fig. 15A. As it follows the spidery terrain, it is conceivable that it is linked with surface activity. The CBRC output in Fig. 21 highlights with the blue channel ice, fog and atmospheric features, while the green and red channels are indicators of dust, soil and rock compositions (through sensitivity to ferric oxides Fe^{3+} and ferrous oxide Fe^{2+}). The cyan coloured features (mixture between red, green and blue i.e. atmospheric with dust components) are suitable candidates for resulting from jet activity. The purple area (blue and red i.e. ice/frost and dust) would suggest a surface where ice and dust are intertwined.

4. Conclusions and discussion

A variety of dark spots was observed on several CaSSIS acquisitions. All spot morphologies discussed in this paper are shown in Fig. 2 and organised into categories as shown in Fig. 3. Their classification was purely based on visual albedo/colour difference seen between units. The list of this classification is as so: (A) dark spot, (B) bright-haloed spot, (C) ringed spot, (D) inverted spot, (E) dark-haloed spot, (F) banded spot, and (G) bright spot.

Fig. 2 shows that in some areas, various types of spots coexist, which brings complexity to our understanding of the evolution of spots. Fig. 22 proposes a putative chronology of the evolution of southern polar spots in terms of morphology, brightness and colour. Following the Kieffer model, several options are possible and interpretations are based on the observations presented here. Further orbital studies of recurring spots will confirm or contradict parts of our hypotheses and will provide insights on latitudinal and/or longitudinal dependencies. The chronology can be established as followed: at the end of winter, spots appear mostly inverted or ringed (see Fig. 2A-B). A small number of bright spots have been observed in Fig. 2E alongside inverted, ringed and bright haloed spots. The distinction between bright spots and inverted is not clear as the dark border producing the strongest contrast can still be quite faint. As bright spots are only seen during the end of Winter and the first period of spring, they are believed to be the first to appear. It could be manifesting small gas ejections and a slight recondensation of cold CO_2 gas onto the cold surface. The inverted spots seem to be preceding ringed spots as the latter are seen with various sized cores. As spring arrives, the spots shift to a bright haloed appearance, as in Fig. 2C-I. Past mid-spring (i.e. Fig. 2.M-P), only plain dark spots without bright haloes remain. The CO_2 ice layer is thought to be very thin. Some spots show darker deposits at their centre, the cause of it is not yet clear as only a handful of spots shows this structure. This darker core surrounded by a dark circum-core (similar to the normal dark spots) is also present in Fig. 2.L with a bright halo. Summer images (i.e. Fig. 2.Q-R) either show remnants of dark spots still displaying contrast with the underlying terrain or a complete blending with the surrounding surface. Fig. 2J shows furthermore a distinctive aspect that differs from ringed spot, as the bright ring appears similar to the neighbouring background. No explanation for this behaviour has been found yet and no other image resembles this one, making it difficult to assess.

When the first rays of sunlight shine through the solid CO_2 layer, dust grains are heated up and sink deeper in the layer (stage preceding the evolution established in Fig. 22). This generates the first jets releasing a

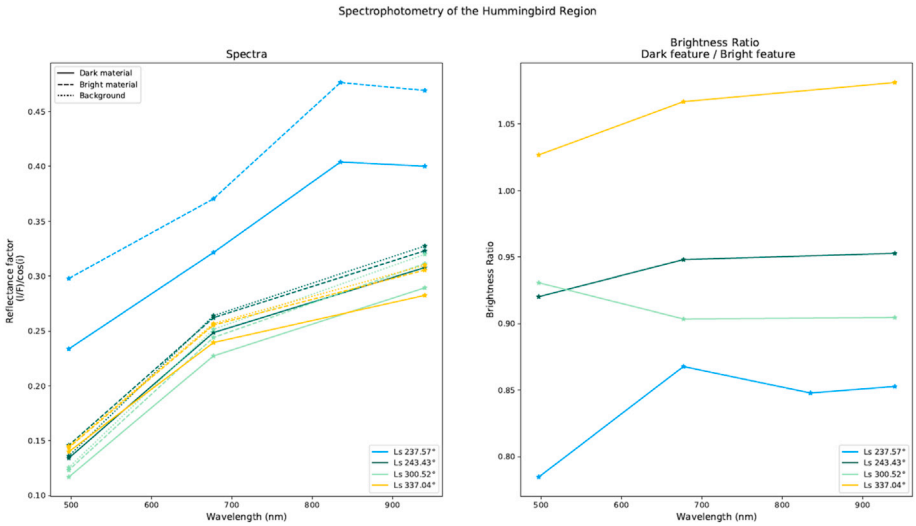

Fig. 16. Spectrophotometry of the Hummingbird images presented in Fig. 15 (A–D). The ratio was made such as the dark component of the ratio is located inside the hummingbird's beak and the bright component is simply the bright terrain surrounding it.

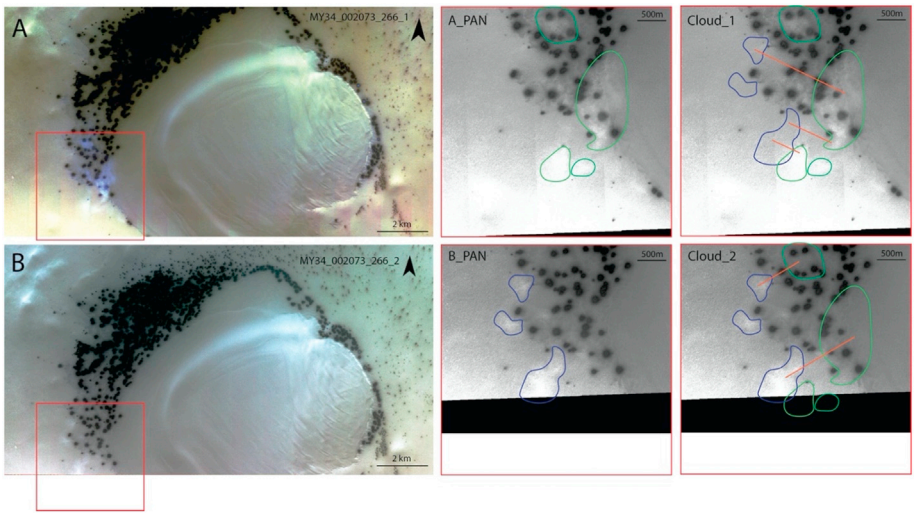

Fig. 17. Stereo acquisition MY34_002073_266 in a small crater located East of Mellish Crater [73°S, 343.3°E]. (A & B) Respectively, stereo #1 with a NIR-PAN-BLU and stereo #2 with a NIR-RED-PAN colour combination and a Gaussian stretch applied. (A_PAN & B_PAN) North is up. Respective zoom in the PAN filter. The green and blue lines highlight the contour of the atmospheric features. (Cloud_1 & Cloud_2) North is up. From stereo #1 to #2 the features have moved, the directions are subject to interpretation and two possibilities are presented here.

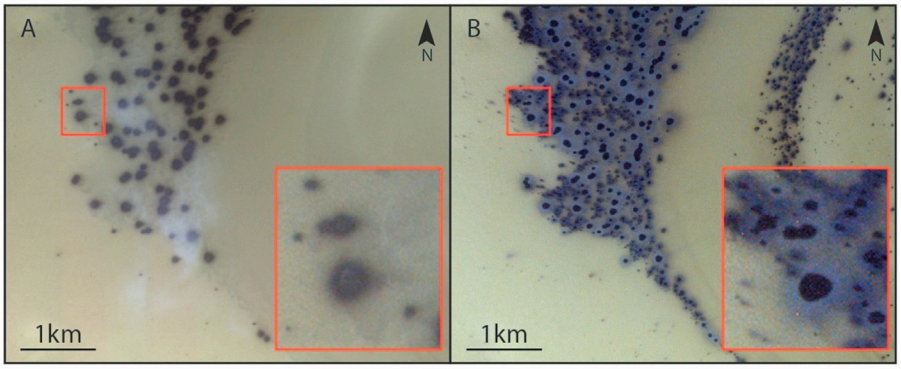

Fig. 18. (A) Image MY34_002073_266_1 taken at L_S 173.96° (sol 361), with a RED-PAN-BLU colour combination. Diffuse atmospheric features are visible on top of spots. (B) Image MY34_002359_267_2 taken at L_S 187.16° (sol 384), with a RED-PAN-BLU colour combination. The atmospheric features have disappeared and the spots have transitioned from ringed spots to bright-haloed spots.

small amount of dust particles onto the surface, they sink immediately back into the icy layer, resulting in a bright spot with low contrast to the surrounding background terrain visible from orbit (Fig. 22 - A1). As the jets grow stronger, they emit more dust particles until there is enough dust to stop light transport into the ice layer. The photometric contrast gets more important as the dust accumulates on the surface, which results

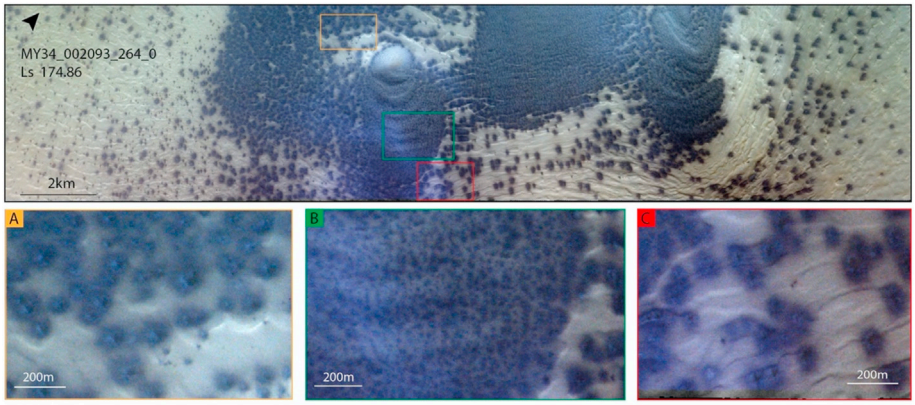

Fig. 19. (Top) Image MY34_002093_264_0 of Burroughs crater before spring Equinox (L_S 174.86°). (Bottom) Sub-image A) Zoom over global spot morphology, with a dark core, and oriented bright halo and a dark uniting halo. Sub-image B) Zoom over the edge of the atmospheric feature. Sub-image C) Singular spot with an inverted appearance visible at the edge of the sub-image.

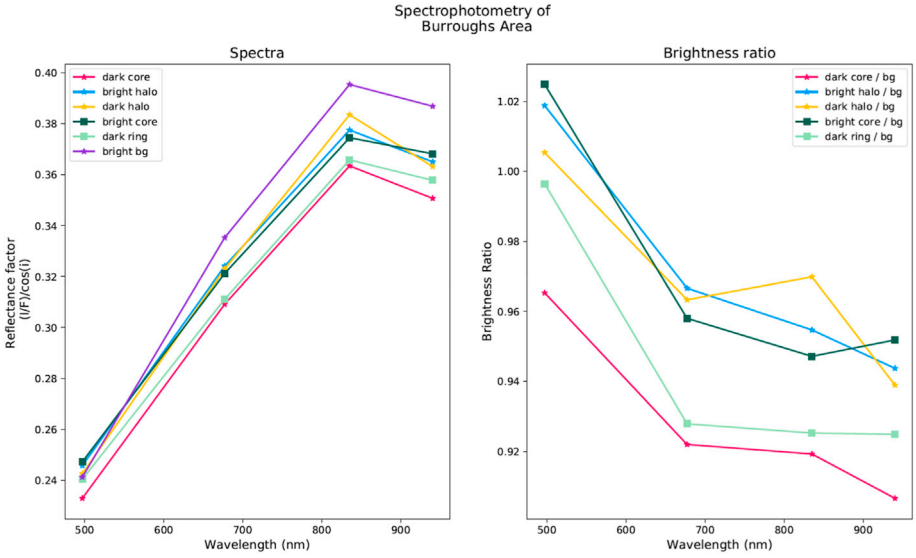

Fig. 20. Spectrophotometry of Burroughs image in Fig. 19. (Left) Spectral plots of ROIs. (Right) Brightness ratio between the ROIs and the background.

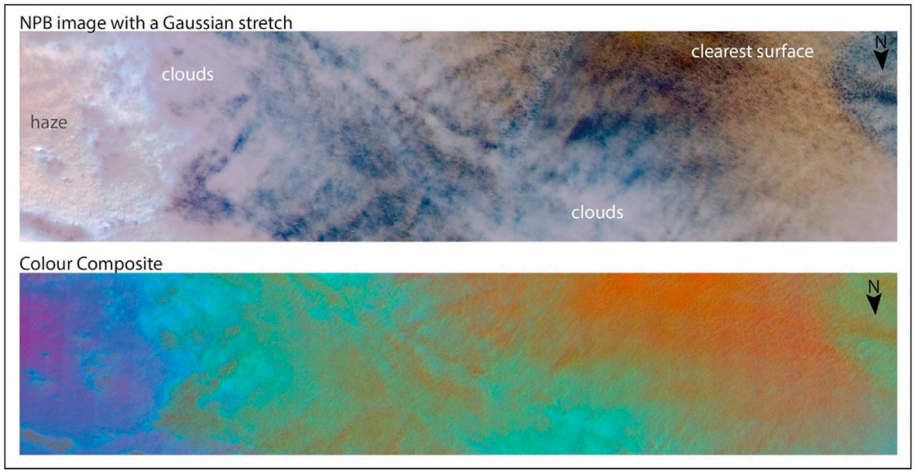

Fig. 21. Cloud visualisation by applying Gaussian stretch and colour band ratio composite of Fig. 15 A at L_S 237.6°. (Top) RGB composite with a global Gaussian stretch applied, enhancing visualisation of the cloud.(Bottom) RGB composite of the ICE/ATM-ALL index (CBRC) with [PAN/BLU], [PAN/NIR] and [Mean(ALL)/(NIR/BLU)] ratios respectively for the R, G and B channels.

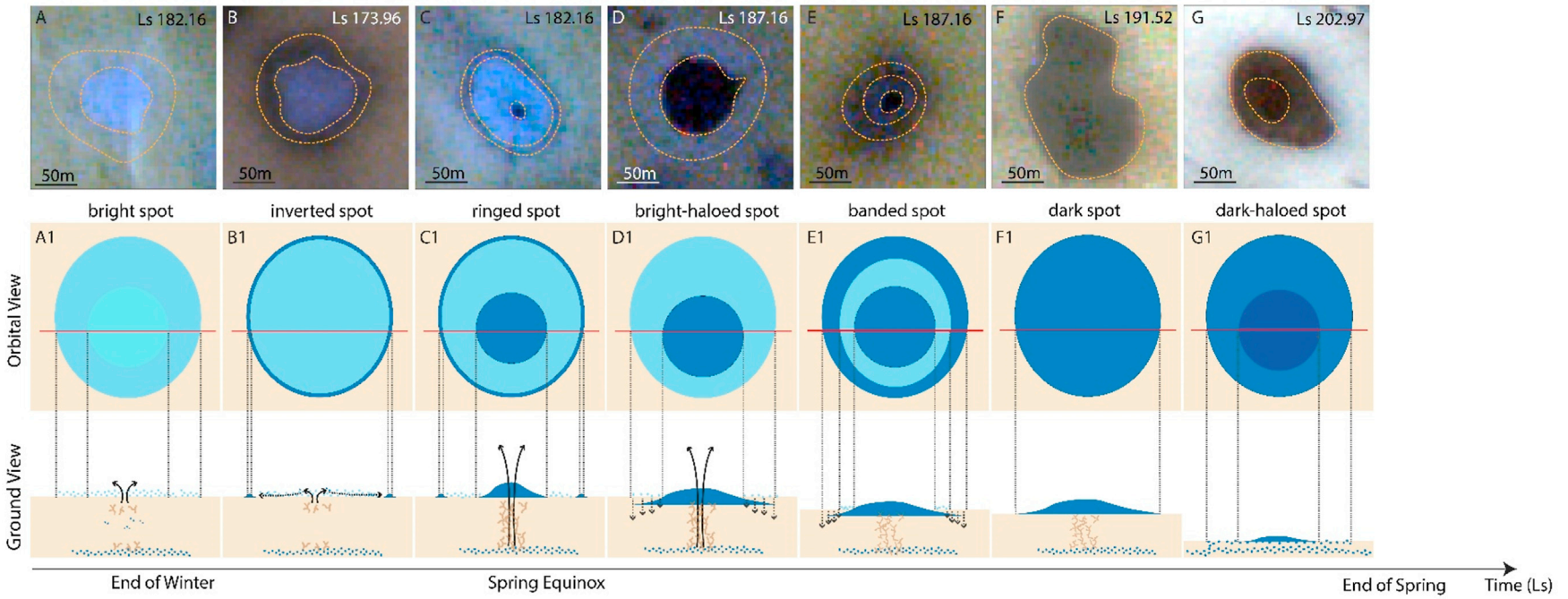

Fig. 22. Sketch of the putative evolution of spots in south polar areas. This figure is based on the Kieffer model (Kieffer, 2000, 2007; Kieffer et al., 2006; Piqueux et al., 2003). The ground view (bottom) represents a possible cross section through the ice. This hypothesis is based on various locations, that could have different evolution period and start, hence could be subject to modifications. The downward dashed arrows represent the sinking of dust particles into the ice, the plain upward arrows the emission of gas vent, the dark blue dots are dust/sand particles and the brown lines inside the ice layer cracks into the ice creating weaknesses for the gas to escape. The horizontal dashed arrows (B1 ground view) indicates a dust movement on top of the ice induced by CO_2 gas pushing away the particles from the centre of the feature.

in visible dark spots (Fig. 22 panels C1 through G1). Since the majority of the dust is deposited at the centre, the thinner layer of particles, located at the edge of the spots, sinks more easily hence creating a bright halo surrounding spots (Fig. 22 panels C1, D1, E1 & G1). Inverted spots (Fig. 22 - B1) are assumed to originate from a dust movement due to gas release at the center of the feature. The dust being pushed away, settles at the outer ring of the feature creating a stronger contrast.

From the spectrophotometric analysis, we do not see major differences between inverted spots (Fig. 22 - B1) at the end of Winter and the bright haloes from bright-haloed spots (Fig. 22 - D1) seen in early spring. The same goes for dark spots in mid-spring. A general shift is observed for the NIR, RED and PAN filters, and a slight difference is seen in the BLU filter. CRISM and HiRISE studies (Pommerol et al., 2011) have shown that blue haloes have the same colour and spectra than the dark dust, which is consistent with dark dust seen through the ice slab. CaSSIS confirms this shift in spectral data and a common physical origin.

CaSSIS here provides key input with its colour combinations and refines the search of active jets by allowing visualisation of atmospheric phenomena possibly in relation with cold jets. Figs. 15, Figs. 17 and 19 all show the presence of atmospheric diffuse features in areas covered in seasonal spots or spiders (enhanced by Gaussian stretches and the CBRC).

A special observation campaign will be planned for the upcoming southern spring (February 2022) to acquire images before the spring equinox in regions where diffuse atmospheric features have been observed. This monitoring will allow a better constrain on the temporal evolution of spots, give insights on the early stages of spot formation and their link with atmospheric phenomena. This objective aligns well with TGO and CaSSIS mission objectives linking atmospheric features with surface activity.

CRediT author statement

Camila Cesar: Conceptualization, Methodology, Investigation, Software, Writing - Original Draft, Writing - Review & Editing, Visualisation.

Antoine Pommerol: Conceptualization, Methodology, Writing - Review & Editing, Resources, Supervision.

Nicolas Thomas: Conceptualization, Methodology, Writing - Review & Editing, Resources, Supervision, Funding Acquisition.

Ganna Portyankina: Writing - Review & Editing.

Candice Hansen: Writing - Review & Editing.

Livio Tornabene: Resources, Writing - Review.

Giovanni Munaretto: Resources, Writing - Review.

Gabriele Cremonese: Funding Acquisition.

Declaration of competing interest

The authors declare that they have no known competing financial interests or personal relationships that could have appeared to influence the work reported in this paper.

Acknowledgements

CaSSIS is a project of the University of Bern and funded through the Swiss Space Office via ESA's PRODEX programme. The instrument hardware development was also supported by the Italian Space Agency (ASI) (ASI-INAF agreement 2020-17-HH.0), INAF/Astronomical Observatory of Padova, and the Space Research Center (CBK) in Warsaw. Support from SGF (Budapest), the University of Arizona (Lunar and Planetary Lab.) and NASA are also gratefully acknowledged. Operations support from the UK Space Agency under grant ST/R003025/1 is also acknowledged. LLT wishes to personally acknowledge funding and support from the Canadian Space Agency (CSA) through their Planetary and Astronomy Missions Co-Investigator programme (19PACOI07) and the Canadian NSERC Discovery Grant programme (RGPIN 2020–06418).

Appendix A. Supplementary data

Supplementary data to this article can be found online at https://doi.org/10.1016/j.pss.2022.105593.

References

Aharonson, O., Zuber, M.T., Smith, D.E., Neumann, G.A., Feldman, W.C., Prettyman, T.H., 2004. Depth, distribution, and density of CO2 deposition on Mars. J. Geophys. Res.: Planets 109. https://doi.org/10.1029/2003JE002223.

Almeida, M., Read, M., Thomas, N., Cremonese, G., Becerra, P., Borrini, G., Gruber, M., Heyd, R., Marriner, C., McArthur, G., McEwen, A., Pommerol, A., Perry, J., Schaller, C., This Issue. Targeted Planning on Mars with ExoMars/CaSSIS. PSS.

Daubar, I.J., Dundas, C.M., Byrne, S., Geissler, P., Bart, G.D., McEwen, A.S., Russell, P.S., Chojnacki, M., Golombek, M.P., 2016. Changes in blast zone albedo patterns around new martian impact craters. Icarus 267, 86–105. https://doi.org/10.1016/j.icarus.2015.11.032.

de Villiers, S., Nermoen, A., Jamtveit, B., Mathiesen, J., Meakin, P., Werner, S.C., 2012. Formation of Martian araneiforms by gas-driven erosion of granular material. Geophys. Res. Lett. 39. https://doi.org/10.1029/2012GL052226.

Hansen, C., Conway, S., Portyankina, G., Thomas, N., McEwen, A., Perry, J., Pommerol, A., Cesar, C., 2019. Searching for Seasonal Jets on Mars in CaSSIS and HiRISE Images 2019. EPSC-DPS2019-388.

Hansen, C.J., Conway, S., Portyankina, G., Thomas, N., McEwen, A.S., 2020. Searching for Seasonal Jets on Mars in CaSSIS and HiRISE Images 2351.

Hansen, C.J., Schwamb, M.E., Portyankina, G., Aye, K.-M., 2017. Planet four: terrains - araneiform in the south polar region of Mars. In: Presented at the 48th Lunar and Planetary Science Conference. Lunar and Planetary Institute, Houston. Abstract #2812.

Hansen, C.J., Thomas, N., Portyankina, G., McEwen, A., Becker, T., Byrne, S., Herkenhoff, K., Kieffer, H., Mellon, M., 2010. HiRISE observations of gas sublimation-driven activity in Mars' southern polar regions: I. Erosion of the surface. Icarus, MRO/HiRISE Studies of Mars 205, 283–295. https://doi.org/10.1016/j.icarus.2009.07.021.

Hao, J., Michael, G.G., Adeli, S., Jaumann, R., 2019. Araneiform terrain formation in angustus labyrinthus, Mars. Icarus 317, 479–490. https://doi.org/10.1016/j.icarus.2018.07.026.

Hao, J., Michael, G.G., Adeli, S., Jaumann, R., Portyankina, G., Hauber, E., Millot, C., Zuschneid, W., 2020. Variability of spider spatial configuration at the Martian south pole. Planet. Space Sci. 185, 104848. https://doi.org/10.1016/j.pss.2020.104848.

Journel, A.G., Huijbregts, C.J., 1976. Mining Geostatistics.

Kaufmann, E., Hagermann, A., 2017. Experimental investigation of insolation-driven dust ejection from Mars' CO2 ice caps. Icarus 282, 118–126. https://doi.org/10.1016/j.icarus.2016.09.039.

Kieffer, H.H., 2007. Cold jets in the Martian polar caps. J. Geophys. Res.: Planets 112. https://doi.org/10.1029/2006JE002816.

Kieffer, H.H., 2000. Annual Punctuated CO2 Slab-Ice and Jets on Mars, vol. 93.

Kieffer, H.H., Christensen, P.R., Titus, T.N., 2006. CO 2 jets formed by sublimation beneath translucent slab ice in Mars' seasonal south polar ice cap. Nature 442, 793–796. https://doi.org/10.1038/nature04945.

Kieffer, H.H., Titus, T.N., Mullins, K.F., Christensen, P.R., 2000. Mars south polar spring and summer behavior observed by TES: seasonal cap evolution controlled by frost grain size. J. Geophys. Res.: Planets 105, 9653–9699. https://doi.org/10.1029/1999JE001136.

Mangold, N., 2005. High latitude patterned grounds on Mars: classification, distribution and climatic control. Icarus, Mars Polar Sci. III 174, 336–359. https://doi.org/10.1016/j.icarus.2004.07.030.

Mangold, N., Maurice, S., Feldman, W.C., Costard, F., Forget, F., 2004. Spatial relationships between patterned ground and ground ice detected by the Neutron Spectrometer on Mars. J. Geophys. Res.: Planets 109. https://doi.org/10.1029/2004JE002235.

Martínez, G.M., Renno, N.O., Elliott, H.M., 2012. The evolution of the albedo of dark spots observed on Mars polar region. Icarus 221, 816–830. https://doi.org/10.1016/j.icarus.2012.09.008.

Mc Keown, L., McElwaine, J.N., Bourke, M.C., Sylvest, M.E., Patel, M.R., 2021. The formation of araneiforms by carbon dioxide venting and vigorous sublimation dynamics under martian atmospheric pressure. Sci. Rep. 11, 6445. https://doi.org/10.1038/s41598-021-82763-7.

Mc Keown, L.E., Bourke, M.C., McElwaine, J.N., 2017. Experiments on sublimating carbon dioxide ice and implications for contemporary surface processes on Mars. Sci. Rep. 7, 14181. https://doi.org/10.1038/s41598-017-14132-2.

Montabone, L., Forget, F., Millour, E., Wilson, R.J., Lewis, S.R., Cantor, B., Kass, D., Kleinböhl, A., Lemmon, M.T., Smith, M.D., Wolff, M.J., 2015. Eight-year climatology of dust optical depth on Mars. Icarus, Dyn. Mars 251, 65–95. https://doi.org/10.1016/j.icarus.2014.12.034.

Montabone, L., Spiga, A., Kass, D., Kleinböhl, A., Forget, F., Millour, E., 2020. Martian year 34 column dust climatology from Mars climate sounder observations : reconstructed maps and model simulations. J. Geophys. Res.: Planets 125, e2019JE006111. https://doi.org/10.1029/2019JE006111.

Munaretto, G., Pajola, M., Cremonese, G., Re, C., Lucchetti, A., Simioni, E., McEwen, A.S., Pommerol, A., Becerra, P., Conway, S.J., Thomas, N., Massironi, M., 2020. Implications for the origin and evolution of martian recurring slope lineae at hale crater from CaSSIS observations. Planet. Space Sci. 187, 104947. https://doi.org/10.1016/j.pss.2020.104947.

Munaretto, G., Pajola, M., Lucchetti, A., Cremonese, G., Simioni, E., Re, C., Bertoli, S., Tornabene, L.L., McEwen, A., Becerra, P., Rangarajan, V.G., Valantinas, A., Portyankina, G., Thomas, N., 2022. Multiband photometry of Martian Recurring Slope Lineae (RSL) and dust-removed features at Horowitz crater, Mars from TGO/CaSSIS color observations. Planet. Space Sci., 105443. In this issue. https://doi.org/10.1016/j.pss.2022.105443.

Munaretto, G., Pajola, M., Lucchetti, A., Re, C., Cremonese, G., Simioni, E., Cambianica, P., Thomas, N., 2021. Topographic correction of HiRISE and CaSSIS images: validation and application to color observations of Martian albedo features. Planet. Space Sci. 200, 105198. https://doi.org/10.1016/j.pss.2021.105198.

Perry, J., Heyd, R., Read, M., Tornabene, L.L., Sutton, S., Byrne, S., Thomas, N., Fennema, A., McEwen, A., Berry, K., This issue. Geometry Pipeline for TGO CaSSIS Observations. Planet. Space Sci..

Pilorget, C., Forget, F., Millour, E., Vincendon, M., Madeleine, J.B., 2011. Dark spots and cold jets in the polar regions of Mars: new clues from a thermal model of surface CO2 ice. Icarus 213, 131–149. https://doi.org/10.1016/j.icarus.2011.01.031.

Piqueux, S., Byrne, S., Richardson, M.I., 2003. Sublimation of Mars's southern seasonal CO2 ice cap and the formation of spiders. J. Geophys. Res.: Planets 108. https://doi.org/10.1029/2002JE002007.

Piqueux, S., Christensen, P.R., 2008. North and south subice gas flow and venting of the seasonal caps of Mars: a major geomorphological agent. J. Geophys. Res.: Planets 113. https://doi.org/10.1029/2007JE003009.

Pommerol, A., Portyankina, G., Thomas, N., Aye, K.-M., Hansen, C.J., Vincendon, M., Langevin, Y., 2011. Evolution of south seasonal cap during martian spring: insights from high-resolution observations by HiRISE and CRISM on Mars reconnaissance orbiter. J. Geophys. Res.: Planets 116. https://doi.org/10.1029/2010JE003790.

Pommerol, A., Thomas, N., Almeida, M., Read, M., Becerra, P., Cesar, C., Valantinas, A., Simioni, E., McEwen, A., Perry, J., Marriner, C., Munaretto, G., Pajola, M., Da Deppo, V., Re, C., Cremonese, G., This issue. In-Flight radiometric calibration of the ExoMars TGO colour and stereo surface imaging System. Planet. Space Sci..

Portyankina, G., Hansen, C.J., Aye, K.-M., 2017. Present-day erosion of Martian polar terrain by the seasonal CO2 jets. Icarus 282, 93–103. https://doi.org/10.1016/j.icarus.2016.09.007.

Portyankina, G., Markiewicz, W.J., Thomas, N., Hansen, C.J., Milazzo, M., 2010. HiRISE observations of gas sublimation-driven activity in Mars' southern polar regions: III. Models of processes involving translucent ice. Icarus, MRO/HiRISE Studies of Mars 205, 311–320. https://doi.org/10.1016/j.icarus.2009.08.029.

Portyankina, G., Pommerol, A., Aye, K.-M., Hansen, C.J., Thomas, N., 2012. Polygonal cracks in the seasonal semi-translucent CO2 ice layer in Martian polar areas. J. Geophys. Res.: Planets 117. https://doi.org/10.1029/2011JE003917.

Schaefer, E.I., McEwen, A.S., Sutton, S.S., 2019. A case study of recurring slope lineae (RSL) at Tivat crater: implications for RSL origins. Icarus 317, 621–648. https://doi.org/10.1016/j.icarus.2018.07.014.

Schwamb, M.E., Aye, K.-M., Portyankina, G., Hansen, C.J., Allen, C., Allen, S., Calef III, F.J., Duca, S., McMaster, A., Miller, G.R.M., 2018. Planet four: terrains - Discovery of araneiforms outside of the south polar layered deposits. Icarus 308, 148–187. https://doi.org/10.1016/j.icarus.2017.06.017.

Thomas, N., Cremonese, G., Ziethe, R., Gerber, M., Brändli, M., Bruno, G., Erismann, M., Gambicorti, L., Gerber, T., Ghose, K., Gruber, M., Gubler, P., Mischler, H., Jost, J., Piazza, D., Pommerol, A., Rieder, M., Roloff, V., Servonet, A., Trottmann, W., Uthaicharoenpong, T., Zimmermann, C., Vernani, D., Johnson, M., Pelò, E., Weigel, T., Viertl, J., De Roux, N., Lochmatter, P., Sutter, G., Casciello, A., Hausner, T., Ficai Veltroni, I., Da Deppo, V., Orleanski, P., Nowosielski, W., Zawistowski, T., Szalai, S., Sodor, B., Tulyakov, S., Troznai, G., Banaskiewicz, M., Bridges, J.C., Byrne, S., Debei, S., El-Maarry, M.R., Hauber, E., Hansen, C.J., Ivanov, A., Keszthelyi, L., Kirk, R., Kuzmin, R., Mangold, N., Marinangeli, L., Markiewicz, W.J., Massironi, M., McEwen, A.S., Okubo, C., Tornabene, L.L., Wajer, P., Wray, J.J., 2017. The colour and stereo surface imaging System (CaSSIS) for the ExoMars trace gas orbiter. Space Sci. Rev. 212, 1897–1944. https://doi.org/10.1007/s11214-017-0421-1.

Thomas, N., Hansen, C.J., Portyankina, G., Russell, P.S., 2010. HiRISE observations of gas sublimation-driven activity in Mars' southern polar regions: II. Surficial deposits and their origins. Icarus, MRO/HiRISE Studies of Mars 205, 296–310. https://doi.org/10.1016/j.icarus.2009.05.030.

Thomas, N., Pommerol, A., Cremonese, G., Simioni, E., This issue. Absolute calibration of the colour and stereo surface imaging System (CaSSIS). Planet. Space Sci..

Thomas, N., Portyankina, G., Hansen, C.J., Pommerol, A., 2011a. HiRISE observations of gas sublimation-driven activity in Mars' southern polar regions: IV. Fluid dynamics models of CO2 jets. Icarus 212, 66–85. https://doi.org/10.1016/j.icarus.2010.12.016.

Thomas, N., Portyankina, G., Hansen, C.J., Pommerol, A., 2011b. Sub-surface CO2 gas flow in Mars' polar regions: gas transport under constant production rate conditions. Geophys. Res. Lett. 38. https://doi.org/10.1029/2011GL046797.

Titus, T.N., Kieffer, H.H., Langevin, Y., Murchie, S., Seelos, F., Vincendon, M., 2007. Bright fans in Mars cryptic region caused by adiabatic cooling of CO2 gas jets. AGU Fall Meet. Abstr. 2007. P24A-05.

Titus, T.N., Kieffer, H.H., Mullins, K.F., 1998. TES Observ. South Pole 30, 20, 05.

Tornabene, L.L., Seelos, F.P., Pommerol, A., Thomas, N., Caudill, C.M., Becerra, P., Bridges, J.C., Byrne, S., Cardinale, M., Chojnacki, M., Conway, S.J., Cremonese, G., Dundas, C.M., El-Maarry, M.R., Fernando, J., Hansen, C.J., Hansen, K., Harrison, T.N., Henson, R., Marinangeli, L., McEwen, A.S., Pajola, M., Sutton, S.S., Wray, J.J., 2018. Image simulation and assessment of the colour and spatial capabilities of the colour and stereo surface imaging System (CaSSIS) on the ExoMars trace gas orbiter. Space Sci. Rev. 214, 18. https://doi.org/10.1007/s11214-017-0436-7.